Stability of $Ca(OH)_2$ at Earth's deep lower mantle conditions

Sen Shao,[1,2] Jingkai Bi,[1] Pengyue Gao,[1,2] Guangtao Liu,[2] Mi Zhou,[2] Jian Lv,[1,2] Yu Xie,[1,2,3,*] and Yanchao Wang[1,2,†]

[1]*State Key Laboratory of Superhard Materials, College of Physics, Jilin University, Changchun 130012, China*

[2]*International Center for Computational Method and Software, College of Physics, Jilin University, Changchun 130012, China*

[3]*Key Laboratory of Physics and Technology for Advanced Batteries (Ministry of Education), College of Physics, Jilin University, Changchun 130012, China*

(Received 24 October 2020; revised 16 April 2021; accepted 24 May 2021; published 14 July 2021)

In this paper, we report that $Ca(OH)_2$, portlandite, is predicted to be stable up to 100 GPa via an unbiased structural search method combined with first-principles calculations. Two pressure-induced structures with $P2_1/c$ and *Pnma* symmetry are proposed at high pressure. The monoclinic $P2_1/c$ structure is the most stable phase after 23 GPa and will undergo a phase transition into a *Pnma* phase at 78 GPa and 0 K. This phase transition is computed to occur at lower pressure as the temperature increases. The high-pressure phases of $Ca(OH)_2$ that we proposed are stable against decomposition into CaO and H_2O at the conditions corresponding to lower mantle geotherms. Our results shed light on the possible presence of $Ca(OH)_2$ in the Earth's mantle as well as its water transportation in the Earth's interior.

DOI: 10.1103/PhysRevB.104.014107

I. INTRODUCTION

$Ca(OH)_2$ is one of the simplest models of hydrous minerals. At ambient conditions, $Ca(OH)_2$ adopts a layered structure with $P\bar{3}m1$ symmetry, which is the prototype of divalent metal $M(OH)_2$ (M = Mg, Mn, Fe, etc.) [1–6], consisting of divalent cations M^{2+} and OH^- ions arranged in layers. However, the high-pressure phases of $Ca(OH)_2$ have long been a puzzle in experiments. Early works reported that $Ca(OH)_2$ became amorphous or partially amorphized under pressure, evidenced by the disappearance of x-ray diffraction (XRD) peaks during the pressure loading process [7–9]. A later study showed that the structural behavior of hydrous compounds could be sensitive to local deviatoric stress, which is considered responsible for observing amorphous $Ca(OH)_2$ [10]. The first high-pressure crystalline phase of $Ca(OH)_2$ (phase II) was synthesized at 7 GPa and 473 K under quasihydrostatic pressure conditions [11,12]. Phase II is a three-dimensional structure with the space group of $P2_1/c$. Almost at the same time, another high-pressure crystalline phase (phase II′) with $C2$ symmetry was prepared at 6–8 GPa and room temperature, which is considered to be a metastable phase existing as an intermediate phase between phase I and phase II, where the detailed atomic occupations of this structure were determined 17 years later [9,13–15]. Although there are many experiments working on the high-pressure properties of $Ca(OH)_2$, the studied pressure range was no higher than 30 GPa. It is still unclear whether $Ca(OH)_2$ could be stable and how $Ca(OH)_2$ behaves at higher pressures and temperatures.

Besides the general interest in the high-pressure properties of $Ca(OH)_2$, there also is increasing attention on the stability and properties of hydrous compounds at high-pressure and high-temperature (HPHT) conditions. This is because it has been found that water can be stored in hydrous minerals [16–26], including FeOOH [27,28] and AlOOH [24,25], as OH^- ions at the Earth's mantle conditions, playing an important role in geological activities [29,30]. Since CaO is one of the major components in the Earth's mantle [31], then in the case where $Ca(OH)_2$ is stable at the Earth's deep mantle conditions (<135 GPa and <3700 K), CaO might react with water to form $Ca(OH)_2$, storing water and affecting geophysical properties. Therefore, it is of great interest to explore the stability and properties of $Ca(OH)_2$ under HPHT conditions.

To investigate the high-pressure behavior of $Ca(OH)_2$, we have performed extensive simulations on crystal structures of $Ca(OH)_2$ up to 100 GPa. As a result, our simulations identified two high-pressure phases of $Ca(OH)_2$ with $P2_1/c$ and *Pnma* symmetry, respectively. The monoclinic $P2_1/c$ phase (phase III) is energetically superior to phase II above 23 GPa at 0 K, where the phase transition pressure becomes higher with increasing temperature, such as from 25 GPa at 390 K to 38 GPa at 2380 K. It transforms into the *Pnma* phase (phase IV) after 78 GPa. This phase-transition pressure is found to be lower as the temperature increases. We also found the velocities of phases III and IV are much lower than those of the preliminary reference Earth model (PREM) in a wide range of pressures. Our current results clearly demonstrated the high-pressure behaviors of $Ca(OH)_2$ in the pressure and temperature conditions corresponding to the Earth's lower mantle.

II. COMPUTATIONAL DETAILS

The structures of $Ca(OH)_2$ are predicted based on the unbiased global structure search method with the particle swarm optimization (PSO) algorithm implemented in the CALYPSO code [32–34]. This method is highly efficient in predicting

*xieyu@jlu.edu.cn
†wyc@calypso.cn

stable structures with only the given chemical compositions and has been benchmarked in various known systems [25,35–37]. For this work, CALYPSO structural predictions are performed with simulation cells containing from one to four chemical formula units. Each generation contained 50 structures, and the first generation was produced randomly with symmetry constraints. For a single run of CALYPSO, 2500 structures, in which 40% of the structures are generated randomly, are calculated. The structural relaxation and calculations of electronic properties are performed based on density function theory [38] by using the Vienna *ab initio* simulation package (VASP) code [39] within the Perdew-Burke-Ernzerhof exchange-correlation functional in the generalized gradient approximation [40]. The all-electron projector augmented-wave [41] method has been adopted with $4s^2$, $2s^2 2p^4$, and $1s^1$ treated as valence electrons for Ca, O, and H atoms, respectively. A kinetic energy cutoff of 1000 eV and a dense k-point sampling of the Brillouin zone with a spacing of $2\pi \times 0.03$ Å^{-1} are used to ensure the enthalpy calculations converged within 1 meV/atom.

The Gibbs free energies of the materials were calculated within the framework of a quasiharmonic approximation, where the Gibbs free energies of $Ca(OH)_2$, CaO, and ice VIII were estimated using the frozen phonon method as implemented in PHONOPY [42] and the Gibbs free energy of ice X was estimated using the temperature-dependent effective potential method [43,44] due to the existence of imaginary phonon frequencies below 120 GPa at 0 K [45]. We have also carefully examined the difference between the calculated Gibbs free energy of ice X by PHONOPY and TDEP at 120 GPa to probe the possible systematic errors between them (Fig. S13). The difference is quite small, ~5 meV/atom, indicating it is feasible to construct the P-T phase diagram by mixing the results of these two methods. It should be noticed that ice melts at high temperatures. The Gibbs free energy of liquid water was calculated using the thermodynamic properties and equations of state from previous studies [46–48] (see details in the Supplemental Material [49]). Fukui *et al.* showed that $Ca(OH)_2$ will melt at 11 GPa and room temperature [50], but Catalli *et al.* investigated the high-pressure behavior of $Ca(OH)_2$ up to 26 GPa and room temperature under quasi-hydrostatic conditions and found $Ca(OH)_2$ could maintain crystallinity [10]. Thus we calculated the melting temperature of $Ca(OH)_2$ using the Z method to obtain a rough melting curve (Figs. S9–S12) [51]. The elastic constants C_{ij} were calculated using strain-stress relationships at small strain [52,53], and the isotropic elastic moduli were then derived from the Voigt-Reuss-Hill averaging scheme [54] (see details in the Supplemental Material).

III. RESULTS AND DISCUSSION

we systemically search structures of $Ca(OH)_2$ at 0, 20, 50, 80, and 100 GPa using the CALYPSO package. The predicted structure of phase I ($P\bar{3}m1$) gives excellent agreement with the experimental data at ambient conditions [55], showing the accuracy of our calculations (see Table S1). At a pressure of 5–23 GPa, phase II ($P2_1/c$) synthesized experimentally is the most energetically stable structure. At higher pressure, our

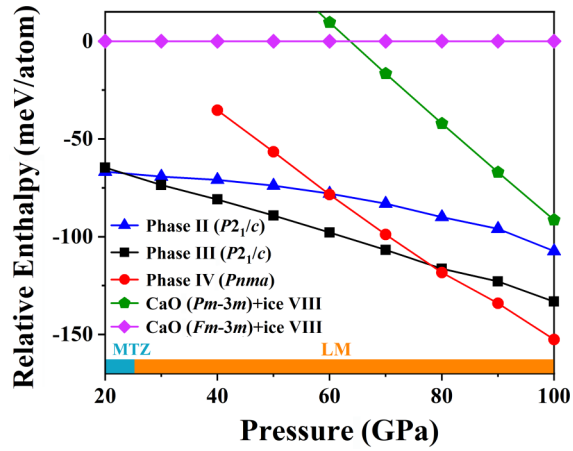

FIG. 1. Enthalpies of various phases for $Ca(OH)_2$ with respect to CaO ($Fm\bar{3}m$) + H_2O (ice VIII) as a function of pressures. The decomposition enthalpies for $Ca(OH)_2$ to CaO ($Pm\bar{3}m$) + H_2O (ice VIII) are also presented. The cyan zone represents the pressure relevant for the mantle transition zone (MTZ), and the orange zone represents the pressure relevant for the lower mantle.

structural predictions uncover two phases, $P2_1/c$ (phase III) and $Pnma$ (phase IV). They are stable against decomposition into CaO and H_2O. The phase transition from phase II to phase III occurs at 23 GPa and 0 K [Fig. 1(a)]. They have a similar structural configuration, consisting of a three-dimensional (3D) network of edge-sharing CaO_7 units and H atoms lying in intervals between CaO_7 units [Figs. S3(c) and S3(e)]. Alternatively, phase II and phase III can also be characterized by the O-H . . . O-H rings lying in different planes. As depicted in Figs. 2(a)–2(d), the O–H . . . O–H rings are lying in (2 3 −2) and (−2 3 2) planes for phase II, while they are lying in (2 3 0) and (−2 3 0) planes for phase III. The arrangements of O-H . . . O-H rings in these phases are likewise different. For phase III, the O atoms on vertices of different directional rings are in lines along the c direction, but for phase II, only the O atoms on vertices of the same directional rings are in lines. The nearest distance of the same directional rings is 6.72 Å in phase II and 6.37 Å in phase III, suggesting phase III is more compact than phase II. In phase III, the length of the O-H bond changes from 0.99 to 1.04 Å and the values of two H-O . . . H angles change from 129.01° to 121.96° and from 81.89° to 88.10°, respectively, as the pressure increases from 23 to 78 GPa. Phase IV becomes the most energetically stable structure above 78 GPa and could be stable at least up to 100 GPa, the highest pressure we studied [Fig. 2(a)]. Pressure induces the break of O-H . . . O-H rings and the formation of O-H . . . O-H chains, of which the main chains are along the b direction and the branches are along the c direction [Figs. 2(e) and 2(f)]. The O-H . . . O-H chains and calcium atoms are coplanar, lying in the ab planes. In this structure, the length of the O-H bond changes from 0.98 to 0.99 Å as the pressure increases from 78 to 100 GPa, while the two H-O . . . H angles change from 157.72° to 158.06° as well as from 86.88° to 71.66°, respectively.

One can see that the volume of $Ca(OH)_2$ (V_{comp}) is significantly reduced by 10.66% when transforming from a layered phase I to the three-dimensional phase II at 5 GPa. As pressure

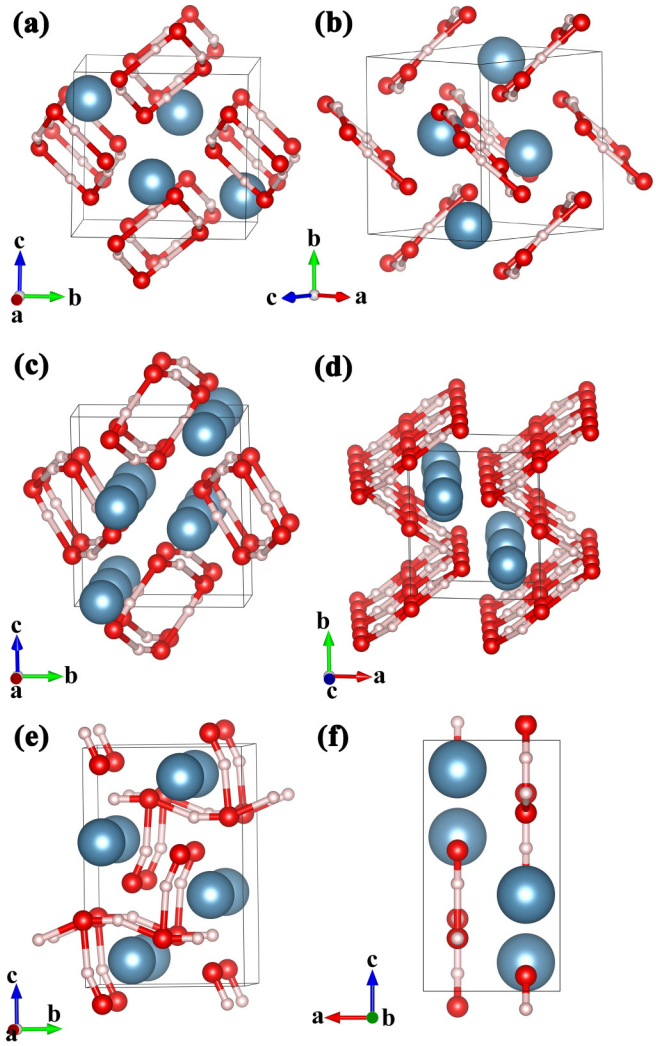

FIG. 2. Crystal structures of $Ca(OH)_2$. (a), (b) Phase II ($P2_1/c$), (c), (d) phase III ($P2_1/c$), and (e), (f) phase IV ($Pnma$). The cyan, red, and pink spheres represent calcium, oxygen, and hydrogen atoms, respectively.

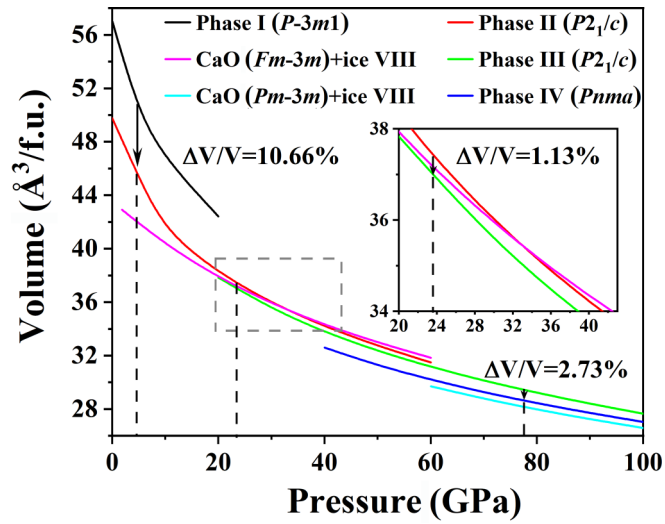

FIG. 3. Equations of state of various phases for $Ca(OH)_2$, CaO ($Fm\bar{3}m$) + H_2O (ice VIII), and CaO ($Pm\bar{3}m$) + H_2O (ice VIII). Vertical dashed lines indicate the transition pressures and arrows are labeled with the calculated volume reduction.

increases, the volume shrinkage of $Ca(OH)_2$ accompanying the phase transition becomes much smaller, which is about 1.13% and 2.73% at 23 and 78 GPa, respectively. Compared to the volumes of decomposition products CaO and ice (V_{decomp}, Fig. 3), we found V_{comp} is always larger than V_{decomp} until $Ca(OH)_2$ transforms into phase III. Interestingly, V_{decomp} becomes smaller than V_{comp} again when pressure is higher than 68 GPa due to the phase transition of CaO from a face-centered-cubic structure to a simple cubic structure. Since both internal energy U and pressure-volume work PV contribute to the enthalpy of materials, the relative thermodynamic stability between $Ca(OH)_2$ and decomposition should be affected by the volume changes, which will be discussed below.

To determine the dynamic stability of high-pressure phases for $Ca(OH)_2$, we calculate the phonon spectra under different pressures. In our simulation, as shown in Fig. S4, the absence of any imaginary phonon frequencies in the whole Brillouin zone suggests that the predicted structures of $Ca(OH)_2$ are dynamically stable.

Moreover, the pressure-dependent O-H vibrational frequencies are of great importance for future experiments to verify the predicted high-pressure structures of $Ca(OH)_2$. Hence, we calculated the O-H vibrational frequencies of $Ca(OH)_2$ at high pressures as shown in Fig. 4. For phase I, there is only one O-H stretch mode, of which the frequency is 111.2 THz at 0 GPa and slightly decreases with increasing pressure. In comparison, the experimentally measured O-H frequency is 108.5 THz at ambient conditions that also decrease at high pressures [10]. The small difference between theory and experiment is probably due to the OH bond length being elongated at 300 K with respect to that at 0 K. All the high-pressure phases of $Ca(OH)_2$ have two O-H stretch modes. For phases II and III, the

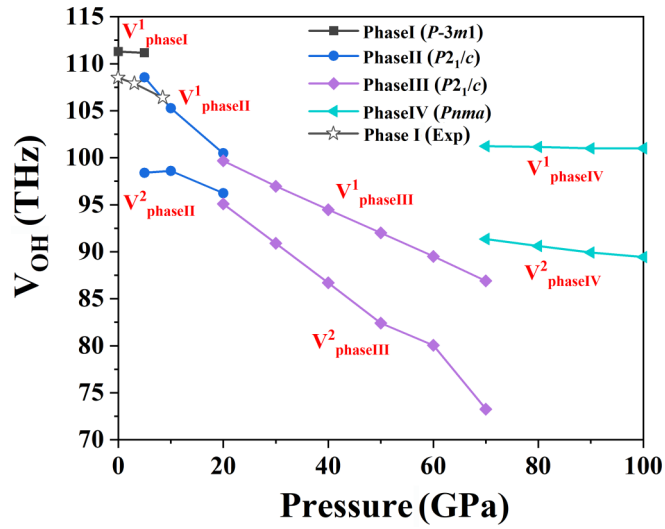

FIG. 4. Calculated O-H stretch frequencies of $Ca(OH)_2$ phases.

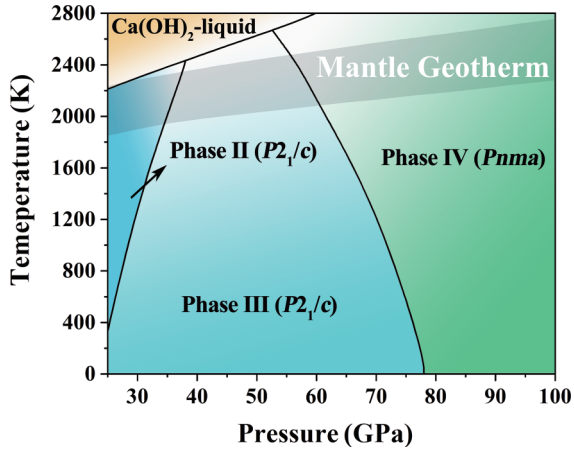

FIG. 5. Computationally derived thermodynamic phase diagram for $Ca(OH)_2$. The gray zone is the mantle geotherm.

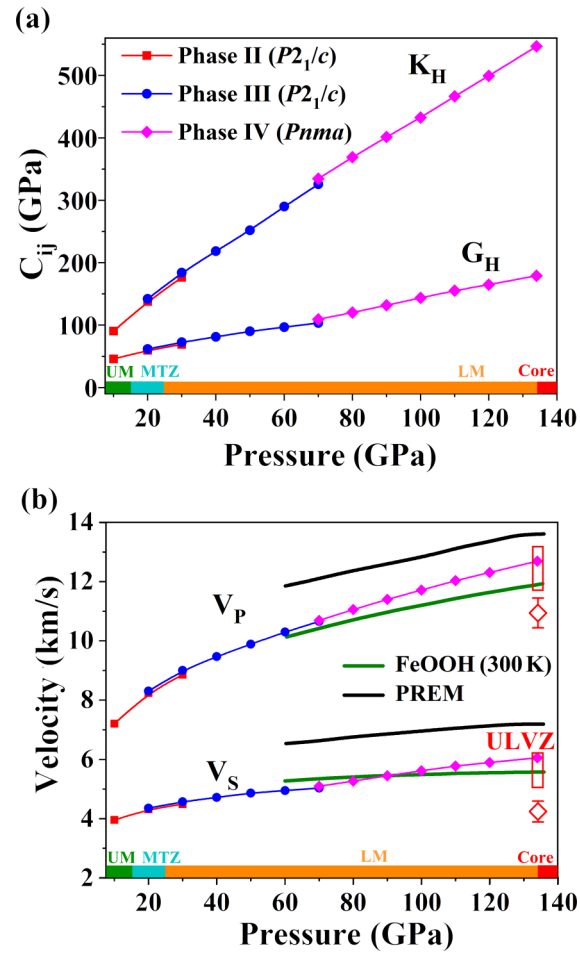

FIG. 6. (a) Hill-averaged bulk (K_H) and shear (G_H) moduli, and (b) wave speeds of P waves (V_P) and S waves (V_S) of different phases for $Ca(OH)_2$ under pressure at 0 K. The dark-green lines represent wave speeds of P waves and S waves of FeOOH at 300 K and open diamonds show FeO_2H_x ($x = 0$–1) extrapolated to 3000 K and CMB pressures [56]. The black lines represent wave speeds of P waves and S waves of PREM. The red rectangles indicate the reduction in V_P (5%–15%) and V_S (15%–30%) observed in ULVZs [57]. The dark-green, cyan, orange, and red zones represent the pressure relevant for the upper mantle (UM), the mantle transition zone (MTZ), the lower mantle (LM), and core, respectively.

O-H vibrational frequencies do not change much at the phase-transition pressures and continue decreasing with increased pressure. A sudden jump to higher frequencies is observed, because the O-H length shortens from 1.04 to 0.98 Å when phase III transforms into phase IV at 78 GPa as we discussed above. Similar to other phases, the frequencies of OH stretching modes decrease slowly again at higher pressures.

Although the hydrous mineral $Ca(OH)_2$ is energetically stable by a large margin compared with the decomposition products CaO and H_2O at 0 K, whether $Ca(OH)_2$ will be thermodynamic stable under HPHT is still uncertain. Determining the stability of $Ca(OH)_2$ under HPHT conditions is essential since the temperature and pressure in the Earth's interior rise significantly as the depth increases. Hence, we calculated Gibbs free energies of these compounds in the quasiharmonic approximation to probe the stability of $Ca(OH)_2$ at the conditions of the lower mantle ($P > 25$ GPa and $T > 1800$ K). The resultant P-T phase diagram is depicted in Fig. 5. $Ca(OH)_2$ is stable at the HPHT conditions of the lower mantle geotherm and do not decompose into CaO and H_2O. When the temperature is above the lower mantle geotherm conditions, $Ca(OH)_2$ will melt (Fig. S12). Phase II is predicted to be stable at the conditions of the mantle transition zone and the top of the lower mantle. Phase III could be stable at relatively low pressure, but the threshold pressure for the thermodynamic stability of phase III increases with increasing temperature, such as going from 25 GPa at 390 K to 38 GPa at 2380 K. It will transform into phase IV (*Pnma*) at 78 GPa and 0 K. This phase transition will shift to lower pressure as the temperature increases. For instance, phase IV becomes stable at 60 GPa above 2100 K.

Seismological studies revealed that there are some seismic velocity discontinuity zones in the Earth's interior [58,59]. For instance, several 5–40 km thick domains lying above the core-mantle boundary (CMB) are called ultralow-velocity zones (ULVZs), where seismic wave speeds are depressed by about 5%–15% for P waves (V_P) and by about 15%–30% for S waves (V_S) [57]. The hydrous mineral, $FeOOH_x$ ($x = 0$–1), which is stable up to the bottom of the lower mantle, is considered as a plausible cause of ULVZs because of its low sound velocities at CMB conditions [56]. Based on our calculations, $Ca(OH)_2$ could be stable in the deep lower mantle. If $Ca(OH)_2$ actually does exist in the Earth's interior, it may also affect the seismic wave velocity. Hence, we calculate the mechanical properties and sound velocities of $Ca(OH)_2$ at the Earth's mantle conditions. The Hill-average bulk (K_H) and shear (G_H) moduli of various phases as a function of pressure are depicted in Fig. 6(a). It is a general rule for all phases of $Ca(OH)_2$ that the values of K_H and G_H increase monotonously with pressure. At 20 GPa, the K_H and G_H are 142.2 and 61.7 GPa for phase III, respectively. This is slightly stiffer than K_H (137.8 GPa) and G_H (59.8 GPa) for phase II at the same pressure. The K_H and G_H of phase IV at 134 GPa are 546.8 and 179.3 GPa, respectively. The wave speeds of P waves (V_P) and S waves (V_S) are depicted in Fig. 6(b). They also increase gradually with the pressure and have maximum values of V_P

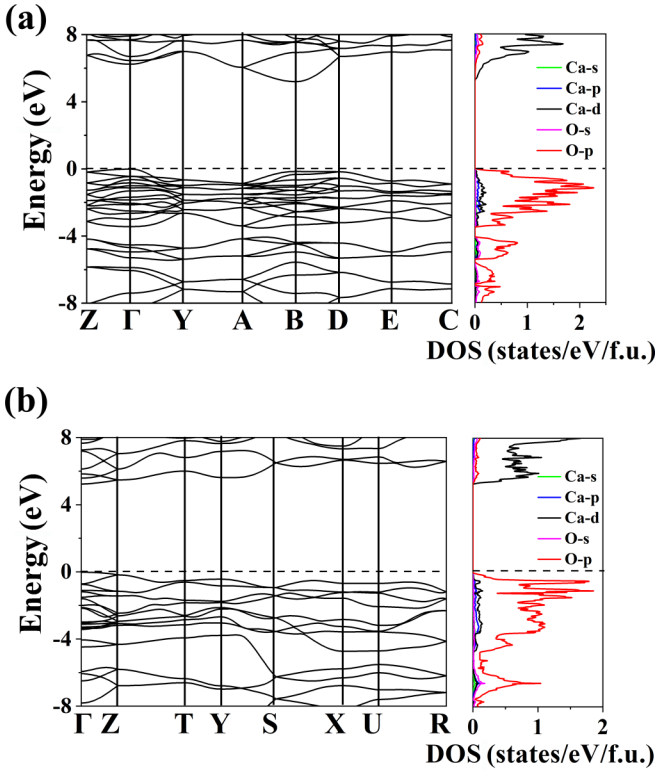

FIG. 7. Calculated electronic band structures (left panel) and DOS (right panel) for (a) phase III ($P2_1/c$) at 40 GPa and (b) phase IV (*Pnma*) at 80 GPa of $Ca(OH)_2$.

(12.6 km/s) and V_S (6.06 km/s) for phase IV at 134 GPa. The wave speeds of $Ca(OH)_2$ are comparable with those of FeOOH at 300 K, which lie within the range of ULVZs and have a significant velocity reduction relative to the radially averaged one-dimensional seismic model PREM [60]. V_P (V_S) will decrease with increasing temperature, which means the wave speeds of $Ca(OH)_2$ might have a large reduction at CMB conditions. If the hydrous mineral $Ca(OH)_2$ is stable at the conditions of CMB and accumulates throughout geological times, it could also have contributions to the formation of ULVZs.

The electronic band structures and the density of states (DOS) of $Ca(OH)_2$ are depicted in Figs. 7 and S5. Phase I is an insulator with a direct band gap of 4.0 eV at ambient conditions and the band gap of phase II is 5.7 eV at 20 GPa. For the predicted phases, the changes in the band gap induced by phase transitions are not conspicuous. Both are wide-gap insulators with the value of the band gap around 5 eV. The H-*s* states are not shown in Fig. 7 by virtue of their small contribution to total DOS, compared to Ca and O. The conduction bands of all phases are mainly dominated by Ca-*d* states and the upper valence bands are mainly contributed by O-*p* states. $Ca(OH)_2$ is an ionic structure, augmented by covalent and hydrogen bonding. The bond length of O-H is 0.97 Å at ambient conditions and varies from 0.98 to 1.04 Å under pressure, which implies there are strong O-H covalent bonds in the high-pressure phases. A calculation of the electron localization function (ELF) is also confirmed the presence of

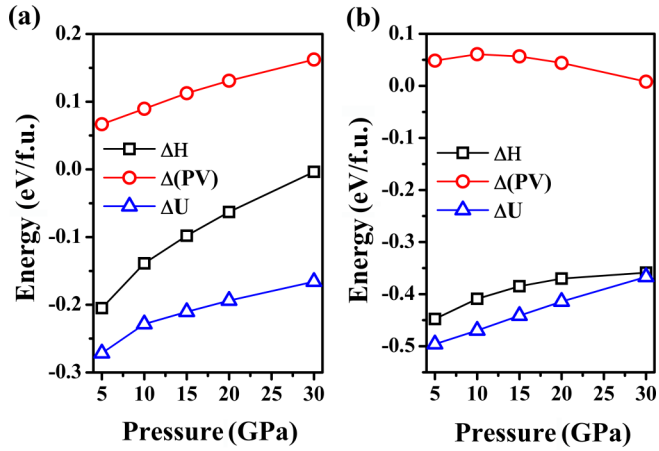

FIG. 8. Calculated ΔH, ΔU, and $\Delta(PV)$ as a function of pressure. (a) $P4_12_12$ phase of $Mg(OH)_2$ relative to MgO and water (ice VIII). (b) Phase II ($P2_1/c$) of $Ca(OH)_2$ relative to CaO and water (ice VIII).

a strong O-H covalent bond in terms of the large occupation between O and H (Fig. S6).

$Mg(OH)_2$ and $Ca(OH)_2$ have the same structure at ambient conditions and will transform into a 3D structure at high pressure. But $Mg(OH)_2$ decomposes into MgO and H_2O at 30 GPa, while $Ca(OH)_2$ is stable at least up to 100 GPa, the highest pressure studied in this work. To elucidate the mechanisms for the pressure-induced phase transitions or decomposition of $Ca(OH)_2$ and $Mg(OH)_2$ under pressure, we probe into the evolution of the internal energy (U) and the product of pressure and volume (PV), since they contribute to the enthalpy ($H = U + PV$) of the pertinent material systems and phases in response to pressure changes. As depicted in Fig. 8(a), we demonstrate the value of ΔU, $\Delta(PV)$, and ΔH as a function of pressure for the $P4_12_12$ phase of $Mg(OH)_2$ relative to MgO and H_2O. The values of ΔU and $\Delta(PV)$ increase with the pressure, leading to ΔH increasing to zero at 30 GPa. Upon further compression, ΔH will become positive, suggesting that $Mg(OH)_2$ decomposes to MgO and H_2O. For $Ca(OH)_2$, we take phase II as an example to elucidate the stability under pressure [Fig. 8(b)]. ΔU of phase II is -0.448 eV at 5 GPa and increases with pressure, while $\Delta(PV)$ of phase II is 0.044 eV at 5 GPa and has a descending trend under compression. The increasing rate of ΔU is slightly larger than the decreasing rate of $\Delta(PV)$, which contributes to a flat increase on ΔH. ΔH of phase II remains negative under pressure, meaning that $Ca(OH)_2$ is stable against decomposition into CaO and H_2O. The ΔU of $P4_12_12$ $Mg(OH)_2$ and phase II of $Ca(OH)_2$ have a similar ascending trend as the pressure increases. Thus, the PV term plays a significant role in the difference of thermodynamic stability for $Mg(OH)_2$ and $Ca(OH)_2$. The descending $\Delta(PV)$ drives that $Ca(OH)_2$ could be stable under higher pressure. The value of ΔU, $\Delta(PV)$, and ΔH for other phases of $Ca(OH)_2$ are depicted in Figs. S7 and S8. ΔU of phase III is negative and has a increasing tendency under pressure. But, due to a dramatic decline of $\Delta(PV)$ under compression, phase III is energetically favorable by a larger margin relative to the decomposition products CaO and H_2O. For phase IV, ΔU and $\Delta(PV)$ have an upward

tendency with increasing pressure. Therefore, both PV and U contribute to the increment of H in phase IV which may result in the decomposition of $Ca(OH)_2$ at sufficient compression.

IV. CONCLUSION

In summary, we propose two high-pressure phases that could be stable at the HPHT conditions of the Earth's lower mantle. Phase III ($P2_1/c$) becomes more stable than phase II after 23 GPa at 0 K and the threshold pressure for the thermodynamic stability of phase III increases with increasing temperature, such as going to 38 GPa at 2380 K. Phase III can be characterized by the O-H $\cdots$ O-H rings along different orientations and the Ca atoms are located in the interstices between these rings. It will transform into a compact phase IV (*Pnma*) after 78 GPa. This phase transition will shift to lower pressure under higher temperatures. The occurrence of the *Pnma* phase leads to the breakup of O-H $\cdots$ O-H rings into chains and the coordination number of Ca increases from seven to eight. The velocities of phase IV are 6.06 km/s (V_S) and 12.6 km/s (V_P) at 134 GPa, much lower than those of PREM. Our results shed light on if $Ca(OH)_2$ does exist in the mantle, it might transport more water into the deep lower mantle and contribute to the formation of ULVZs.

ACKNOWLEDGMENTS

This research was supported by the National Key Research and Development Program of China under Grant No. 2016YFB0201201; the National Natural Science Foundation of China under Grants No. 11404128, No. 11822404, No. 11534003, No. 11974134, No. 11774127, and No. 12022408; Jilin Province Outstanding Young Talents Project (No. 20190103040JH); Program for JLU Science and Technology Innovative Research Team; and the Science Challenge Project No. TZ2016001. Part of the calculation was performed in the high-performance computing center of Jilin University.

[1] A. Pavese, M. Catti, G. Ferraris, and S. Hull, Phys. Chem. Miner. **24**, 85 (1997).
[2] J. Parise, B. Theroux, R. Li, J. Loveday, W. Marshall, and S. Klotz, Phys. Chem. Miner. **25**, 130 (1998).
[3] J. B. Parise, J. S. Loveday, R. J. Nelmes, and H. Kagi, Phys. Rev. Lett. **83**, 328 (1999).
[4] L. Hemmingsen, R. Bauer, M. Bjerrum, K. Schwarz, P. Blaha, and P. Andersen, Inorg. Chem. **38**, 2860 (1999).
[5] R. Cairns and E. Ott, J. Am. Chem. Soc. **55**, 527 (1933).
[6] H. Lutz, H. Möller, and M. Schmidt, J. Mol. Struct. **328**, 121 (1994).
[7] C. Meade and R. Jeanloz, Geophys. Res. Lett. **17**, 1157 (1990).
[8] M. Kruger, Q. Williams, and R. Jeanloz, J. Chem. Phys. **91**, 5910 (1989).
[9] R. Iizuka, H. Kagi, K. Komatsu, D. Ushijima, S. Nakano, A. Sano-Furukawa, T. Nagai, and T. Yagi, Phys. Chem. Miner. **38**, 777 (2011).
[10] K. Catalli, S.-H. Shim, and V. Prakapenka, Geophys. Res. Lett. **35**, L05312 (2008).
[11] M. Kunz, K. Leinenweber, J. Parise, T.-C. Wu, W. Bassett, K. Brister, D. Weidner, M. Vaughan, and Y. Wang, High Press. Res. **14**, 311 (1996).
[12] K. Leinenweber, D. E. Partin, U. Schuelke, M. O'Keeffe, and R. B. Von Dreele, J. Solid State Chem. **132**, 267 (1997).
[13] S. Ekbundit, K. Leinenweber, J. Yarger, J. Robinson, M. Verhelst-Voorhees, and G. Wolf, J. Solid State Chem. **126**, 300 (1996).
[14] R. Iizuka, T. Yagi, K. Komatsu, H. Gotou, T. Tsuchiya, K. Kusaba, and H. Kagi, Am. Mineral. **98**, 1421 (2013).
[15] R. Iizuka, K. Komatsu, H. Kagi, T. Nagai, A. Sano-Furukawa, T. Hattori, H. Gotou, and T. Yagi, J. Solid State Chem. **218**, 95 (2014).
[16] M. Kanzaki, Phys. Earth Planet. Inter. **66**, 307 (1991).
[17] M. Kanzaki, Mineral. J. **16**, 278 (1993).
[18] P. Fumagalli, L. Stixrude, S. Poli, and D. Snyder, Earth Planet. Sci. Lett. **186**, 125 (2001).
[19] S. R. Shieh, H.-k. Mao, R. J. Hemley, and L. C. Ming, Earth Planet. Sci. Lett. **177**, 69 (2000).
[20] J. Tsuchiya, Geophys. Res. Lett. **40**, 4570 (2013).
[21] J. Tsuchiya and K. Umemoto, Geophys. Res. Lett. **46**, 7333 (2019).
[22] S. Ono, Contrib. Mineral. Petrol. **137**, 83 (1999).
[23] A. Sano, E. Ohtani, T. Kubo, and K.-i. Funakoshi, J. Phys. Chem. Solids **65**, 1547 (2004).
[24] T. Kuribayashi, A. Sano-Furukawa, and T. Nagase, Phys. Chem. Miner. **41**, 303 (2014).
[25] X. Zhong, A. Hermann, Y. Wang, and Y. Ma, Phys. Rev. B **94**, 224110 (2016).
[26] L. Zhang, H. Yuan, Y. Meng, and H.-k. Mao, Proc. Natl. Acad. Sci. USA **115**, 2908 (2018).
[27] M. Nishi, Y. Kuwayama, J. Tsuchiya, and T. Tsuchiya, Nature (London) **547**, 205 (2017).
[28] C. Lu and C. Chen, J. Phys. Chem. Lett. **9**, 2181 (2018).
[29] E. Ohtani, Elements **1**, 25 (2005).
[30] E. Ohtani, Annu. Rev. Earth Planet. Sci. **49**, 253 (2021).
[31] T. Yanagi, *Arc Volcano of Japan* (Springer, Berlin, 2011), pp. 9–17.
[32] Y. Wang, J. Lv, L. Zhu, and Y. Ma, Comput. Phys. Commun. **183**, 2063 (2012).
[33] Y. Wang, J. Lv, L. Zhu, and Y. Ma, Phys. Rev. B **82**, 094116 (2010).
[34] B. Gao, P. Gao, S. Lu, J. Lv, Y. Wang, and Y. Ma, Sci. Bull. **64**, 301 (2019).
[35] G. Yang, Y. Wang, F. Peng, A. Bergara, and Y. Ma, J. Am. Chem. Soc. **138**, 4046 (2016).
[36] H. Liu, I. I. Naumov, R. Hoffmann, N. Ashcroft, and R. J. Hemley, Proc. Natl. Acad. Sci. USA **114**, 6990 (2017).
[37] V. N. Robinson, Y. Wang, Y. Ma, and A. Hermann, Proc. Natl. Acad. Sci. USA **114**, 9003 (2017).
[38] W. Kohn and L. J. Sham, Phys. Rev. **140**, A1133 (1965).
[39] G. Kresse and J. Furthmüller, Phys. Rev. B **54**, 11169 (1996).
[40] J. P. Perdew, J. A. Chevary, S. H. Vosko, K. A. Jackson, M. R. Pederson, D. J. Singh, and C. Fiolhais, Phys. Rev. B **48**, 4978(E) (1993).
[41] P. E. Blöchl, Phys. Rev. B **50**, 17953 (1994).
[42] A. Togo, F. Oba, and I. Tanaka, Phys. Rev. B **78**, 134106 (2008).

[43] O. Hellman, I. A. Abrikosov, and S. I. Simak, Phys. Rev. B **84**, 180301(R) (2011).
[44] O. Hellman, P. Steneteg, I. A. Abrikosov, and S. I. Simak, Phys. Rev. B **87**, 104111 (2013).
[45] R. Caracas, Phys. Rev. Lett. **101**, 085502 (2008).
[46] S. Saxena and Y. Fei, Geochim. Cosmochim. Acta **51**, 783 (1987).
[47] A. Belonoshko and S. Saxena, Geochim. Cosmochim. Acta **55**, 381 (1991).
[48] M. Millot, S. Hamel, J. R. Rygg, P. M. Celliers, G. W. Collins, F. Coppari, D. E. Fratanduono, R. Jeanloz, D. C. Swift, and J. H. Eggert, Nat. Phys. **14**, 297 (2018).
[49] See Supplemental Material at http://link.aps.org/supplemental/10.1103/PhysRevB.104.014107 for the calculation method, structure information, phonon spectrum, and melting curve.
[50] H. Fukui, O. Ohtaka, T. Nagai, T. Katsura, K. Funakoshi, and W. Utsumi, Phys. Chem. Miner. **27**, 367 (2000).
[51] A. B. Belonoshko, N. V. Skorodumova, A. Rosengren, and B. Johansson, Phys. Rev. B **73**, 012201 (2006).
[52] B. B. Karki, L. Stixrude, and R. M. Wentzcovitch, Rev. Geophys. **39**, 507 (2001).
[53] J. F. Nye, *Physical Properties of Crystals: Their Representation by Tensors and Matrices* (Oxford University Press, Oxford, UK, 1985).
[54] R. Hill, Proc. Phys. Soc. A **65**, 349 (1952).
[55] L. Desgranges, D. Grebille, G. Calvarin, G. Chevrier, N. Floquet, and J.-C. Niepce, Acta Crystallogr., Sect. B: Struct. Sci. **49**, 812 (1993).
[56] J. Liu, Q. Hu, D. Y. Kim, Z. Wu, W. Wang, Y. Xiao, P. Chow, Y. Meng, V. B. Prakapenka, H.-K. Mao *et al.*, Nature (London) **551**, 494 (2017).
[57] M. S. Thorne and E. J. Garnero, J. Geophys. Res. **109**, B08301 (2004).
[58] M. Niazi and D. L. Anderson, J. Geophys. Res. **70**, 4633 (1965).
[59] A. E. Ringwood, Phys. Earth Planet. Inter. **3**, 109 (1970).
[60] A. M. Dziewonski and D. L. Anderson, Phys. Earth Planet. Inter. **25**, 297 (1981).